Nanoscale

Accepted Manuscript

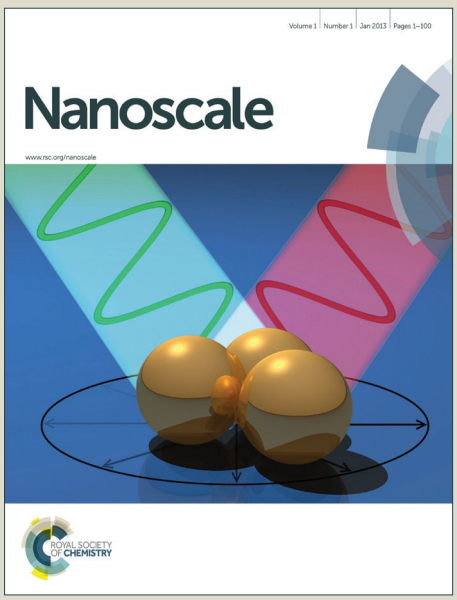

ROYAL SOCIETY OF CHEMISTRY

www.rsc.org/nanoscale

Nanoscale

PAPER

The credible evidence for passivation effect of remnant PbI_2 in $CH_3NH_3PbI_3$ films for improving the performance of perovskite solar cells

Received 00th January 20xx,
Accepted 00th January 20xx

DOI: 10.1039/x0xx00000x

www.rsc.org/

Shimao Wang,[a,b] Weiwei Dong,*[a,b] Xiaodong Fang,*[a,b,c] Qingli Zhang,[a] Shu Zhou,[a] Zanhong Deng,[a,b] Ruhua Tao,[a,b] Jingzhen Shao,[a,b] Rui Xia,[a] Chao Song,[a] Linhua Hu[b] and Jun Zhu[b]

The role of the remnant PbI_2 in $CH_3NH_3PbI_3$ films is still in controversy, some investigations have revealed that the remnant PbI_2 plays a passivation role, reduce the charge recombination in perovskite solar cells (PSCs), and improve the performance of PSCs, but the opposing views state that the remnant PbI_2 has not passivation effect and it would deteriorate the stability of the devices. In our investigation, the $CH_3NH_3PbI_3$ films have been prepared by two-step spin-coating method and the content of the remnant PbI_2 in $CH_3NH_3PbI_3$ films has been tuned through varying the preparation temperature. It has been found that increasing the heating temperature could increase the coverage of spin-coated PbI_2 films which has led to high coverage $CH_3NH_3PbI_3$ films and more remnant PbI_2 in $CH_3NH_3PbI_3$ films, and as a result, the cell performance of PSCs was enhanced obviously and the maximum power conversion efficiency of 14.32±0.28% was achieved by the PSCs prepared at 130/120 °C (PbI_2 films was heated at 130 °C and $CH_3NH_3PbI_3$ films was heated at 120 °C). Furthermore, the dark current, electrochemical impedance spectroscopy and time-resolved fluorescence emission decay measurements revealed that the charge recombination in PSCs has been gradually suppressed and the fluorescence emission lifetime has gradually increased with the content of remnant PbI_2 increasing. Thus, the passivation effects of the unreacted and decomposited PbI_2 for improving the performance of PSCs have been confirmed unquestionably.

Introduction

With the advantages of large absorption coefficients [1], suitable band gap [2], weak exciton binding energy [3], high charge carrier mobilities [4,5] and long carrier diffusion lengths [6,7], organolead halide perovskites ($MAPbX_3$ and $FAPbX_3$, MA = $CH_3NH_3^+$, FA = $NH_2CH{=}NH_2^+$, X = Cl^-, Br^-, or I^-) have been attracting extensive research attention for photovoltaic applications [8–12], since $CH_3NH_3PbI_3$ and $CH_3NH_3PbBr_3$ were used as light harvesters in dye-sensitized solar cell configurations for the first time by Miyasaka and colleagues in 2009 [13]. During the past six years, an explosive growth has occurred in the power conversion efficiency (*PCE*) of perovskite solar cells (PSCs), the *PCE* rapidly increased from 3.8% [13] in 2009 to a certified 21.0% [14] in 2015.

Mesoscopic and planar architectures are the two most widely adopted configurations for PSCs. A typical mesoscopic-PSC consists of TiO_2 compact layer, TiO_2 nanoparticle scaffold layer, perovskite absorber layer, hole-transporting layer (HTL) and metal (Au or Ag) back electrode, and they are successively deposited on a transparent conductive substrate [15]. For planar-PSCs, TiO_2 nanoparticle scaffold layer is absent and the perovskite absorber layers are directly deposited on TiO_2 compact layer. The performance of PSCs strongly depends on the quality of perovskite absorber layer including its crystallinity and morphology and composition [16–20]. Good crystallinity and favourable morphology could enhance the light harvesting and promote charge generation, separation and transportation. Additionally, perovskite films also play another important role to separate electron-transporting layer (ETL, TiO_2 compact and scaffold layer) and HTL, and suppress charge recombination through avoiding the detrimental contact of ETL with HTL, which requires perovskite films to have high compactness and coverage [21,22]. Two-step sequential deposition [23] is a widely accepted method for preparing perovskite films, and it is obvious that the morphology of PbI_2 films has a great influence on the compactness of the obtained $CH_3NH_3PbI_3$ films. Therefore, many efforts have been devoted to preparing dense PbI_2 films for further compact $CH_3NH_3PbI_3$ films preparation [24,25].

Furthermore, the $CH_3NH_3PbI_3$ film prepared trough two-step sequential deposition method generally contains a certain amount of remnant PbI_2. Part of the remnant PbI_2 is the unreacted PbI_2 left in the conversion of PbI_2 to $CH_3NH_3PbI_3$ due

[a] Anhui Provincial Key Laboratory of Photonic Devices and Materials, Anhui Institute of Optics and Fine Mechanics, Chinese Academy of Sciences, Hefei 230031, P. R. China. E-mail: wwdong@aiofm.ac.cn (W. Dong), xdfang@aiofm.ac.cn (X. Fang)
[b] Key Laboratory of Novel Thin Film Solar Cells, Chinese Academy of Sciences, Hefei 230031, P. R. China
[c] School of Environmental Science and Optoelectronic Technology, University of Science and Technology of China, Hefei 230026, P. R. China

† Electronic Supplementary Information (ESI) available: Different magnifications of FE-SEM images and binarized FE-SEM images of the PbI_2 films prepared at different temperature. See DOI: 10.1039/x0xx00000x

to the insufficiency of CH_3NH_3I solution diffusion into PbI_2 films [26–28] and the other forms in the sintering process due to the decomposition of $CH_3NH_3PbI_3$ [29,30]. The unreacted PbI_2 usually forms a passivation layer located between the ETL and $CH_3NH_3PbI_3$ layer and the decomposited PbI_2 usually fills the $CH_3NH_3PbI_3$ grain boundaries, both of them exhibit passivation effects and could reduce the charge recombination at the ETL/perovskite interface and the perovsktie/HTL interface, respectively, and therefore improve the cell performance of PSCs [26–31]. Even for the mixed-cation mixed-halide perovskite films fabricated through a single step from a solution containing a mixture of FAI, PbI_2, MABr, and $PbBr_2$, the excess PbI_2 in the perovskite films also exhibited passivation effect and suppressed the charge recombination at the ETL/perovskite interface, and then pushed the *PCE* of the corresponding PSCs up to 20.8% which is the highest *PCE* of PSCs in the published literatures [32]. However, there are also some diametrically opposed views on the passivation effect of the remnant PbI_2. Some literatures state that the remnant PbI_2 has not passivation effect [33] or it would deteriorate the stability and reproducibility of devices [34–36]. These conflicting opinions mainly caused by the different amount, location and form of the remnant PbI_2 in perovskite films. Therefore, finding more evidences for the passivation effect of remnant PbI_2 in perovskite films and optimizing the amount, location and form of remnant PbI_2 is urgent for device performance improvement.

In this investigation, two-step spin-coating method [37] was adopted to prepare $CH_3NH_3PbI_3$ films on TiO_2 scaffold layers. The heating temperatures of PbI_2 and $CH_3NH_3PbI_3$ films were tuned to improve the morphology of PbI_2 and $CH_3NH_3PbI_3$ films and vary the content of remnant PbI_2 in $CH_3NH_3PbI_3$ films. The effect of heating temperature on the morphology of PbI_2 and $CH_3NH_3PbI_3$ films, the content of remnant PbI_2 in $CH_3NH_3PbI_3$ films and the cell performance of PSCs was investigated. Subsequently, the charge recombination behaviour of PSCs and the passivation effect of remnant PbI_2 were investigated through electrochemical impedance spectroscopy (EIS), dark current and time-resolved fluorescence emission decay measurements.

Experimental

Materials

Lead(II) iodide (PbI_2, 99%) was purchased from Acros Organics. Titanium(IV) isopropoxide (TTIP, 97%) and hydriodic acid (57 wt% in water) were purchased from Sigma-Aldrich. Methylamine solution (40% in methanol) was purchased from TCI. TiO_2 paste (DSL 18NR-T) and FK 102 Co(III) TFSI salt ($Co[PyPz]_3[TFSI]_3$) were from Dyesol. Lithium bis(trifluoromethylsulphonyl)imide (Li-TFSI, 99%), *N*,*N*-dimethylformamide (DMF, 99.5%), 4-*tert*-butylpyridine (TBP, 96%), isopropanol (99.5%) and chlorobenzene (99%) were from Aladdin. 2,2'7,7'-tetrakis(*N*,*N*-di-*p*-methoxyphenylamine)-9,9'-spirobifluorene (spiro-OMeTAD) was from Merck KGaA. Acetonitrile (99.8%), zinc powder (90%), concentrated hydrochloric acid (36–38%), diethyl ether anhydrous (99.7%) and absolute ethanol (99.7%) were from Sinopharm Chemical Reagent Co. Ltd. All the chemicals were used without purification.

Methyl ammonium iodide (CH_3NH_3I) was synthesized according to the reported procedure [19]. Briefly, 27.86 mL methylamine (40% in methanol) was reacted with 30 mL hydroiodic acid (57 wt% in water) in a 250 mL round bottomed flask at 0 °C for 2 h with stirring. The precipitate was recovered by evaporation using a rotary evaporator at 50 °C for 1 h. The product, CH_3NH_3I, was washed with diethyl ether anhydrous by stirring the solution for three times, and then dried at 60 °C in a vacuum oven for 24 h.

Fluorine-doped tin oxide (FTO) conductive substrates (TEC-15, 15 $\Omega \cdot sq^{-1}$, LOF) with dimensions of 20 mm × 13 mm were patterned through etching with Zn powder and 2 M HCl diluted in deionized water. The etched FTO substrates were ultrasonically cleaned in acetone, ethanol, and deionized water for 15 min, respectively, rinsed with deionized water, and then dried in a nitrogen stream.

$CH_3NH_3PbI_3$ films deposition and solar cell fabrication

Preparation of TiO_2 compact and scaffold layers. A TiO_2 compact layer was prepared by spin-coating a mildly acidic solution of TTIP in ethanol on the FTO substrate at 3000 rpm for 30 s, subsequently annealed at 500 °C for 30 min. The mildly acidic solution of TTIP was prepared using TTIP, absolute ethanol and 2 M HCl according to the reported method developed by H. J. Snaith [38]. The TiO_2 scaffold layer was spin-coated at 5000 rpm for 30 s onto the top of the TiO_2 compact layer using the 18NR-T TiO_2 paste diluted in absolute ethanol (1:3.5, weight ratio). After drying at 120 °C for 10 min, the films were annealed at 500 °C for 30 min.

Deposition of $CH_3NH_3PbI_3$ absorber layer. The $CH_3NH_3PbI_3$ layer was prepared through a two-step spin-coating method in a glove box full of dry nitrogen. 1 M PbI_2 solution was obtained by dissolving appropriate PbI_2 powder into DMF under stirring at 70 °C overnight, then the solution was kept at 70 °C during the whole procedure. A 30 μL of PbI_2 solution was spin-coated on TiO_2 scaffold layer successively at 3000 rpm for 18 s and 6000 rpm for 30 s. After drying at room temperature for 18 min, they were heated on a hotplate for 10 min, and the heating temperature was designed to be 90, 100, 110, 120 and 130 °C, respectively. After cooling to room temperature, a 100 μL of CH_3NH_3I solution (10 $mg \cdot mL^{-1}$ in isopropanol) was loaded on PbI_2 coated TiO_2 scaffold films for 20 s to react with PbI_2 and form $CH_3NH_3PbI_3$, subsequently spun at 3000 rpm for 30 s and heated at 90, 100, 110, 120 and 130 °C for 10 min, respectively.

Deposition of HTL and Ag electrode. The HTL was deposited onto the $CH_3NH_3PbI_3$ films through spin-coating a solution of spiro-OMeTAD at 4000 rpm for 30 s. The spiro-OMeTAD solution was prepared by dissolving 72.3 mg spiro-OMeTAD, 28.8 μL of TBP, 17.5 μL of LiTFSI solution (520 $mg \cdot mL^{-1}$ in acetonitrile) and 29 μL of $Co[PyPz]_3[TFSI]_3$ solution (300 $mg \cdot mL^{-1}$ in acetonitrile) in 1 mL of chlorobenzene [23]. After the deposition of an about 80 nm thick silver electrode onto the

HTL through vacuum thermal evaporation, a PSC was obtained. The active area of devices was 9 mm^2 determined using a 3 mm × 3 mm black mask.

Characterization

Morphologies of the samples were characterized using a field-emission scanning electron microscope (FE-SEM, Zeiss Sigma 500, Carl Zeiss, Germany). The coverage of PbI_2 films was estimated from their FE-SEM images using Image J2x software (National Health Institute, USA). The X-ray diffraction (XRD) patterns were recorded using a X-ray diffractometer (Philips X'pert, Holland) with Cu Kα radiation (λ = 0.15418 nm). The ultraviolet-visible-near infrared (UV–Vis–NIR) absorption spectra of $CH_3NH_3PbI_3$ films were measured using an UV–Vis–NIR spectrophotometer (HITACHI, U-3900H, Japan).

The photocurrent-photovoltage (*J–V*) curves of PSCs were measured with a Keithley 2420 digital source meter in backward mode under the illumination of a solar simulator (Newport Oriel 94043A, USA, AM1.5, 100 $mW{\cdot}cm^{-2}$). The incident photon to current efficiency (IPCE) spectra was measured using 300 W Xe lamp light source with monochromatic light in the range of 300–900 nm. EIS measurements were performed on a frequency response analyzer equipped with PGSTAT-30 from Autolab, the PSCs were measured under the bias voltages of 0.7, 0.8, 0.9 and 1.0 V, respectively, in the dark, the frequency range is 10^6 – 1 Hz, and the magnitude of the alternative signal was 10 mV. Linear Sweep Voltammetry (LSV) curves of the PSCs were measured in the dark to obtain the dark current with the same instrument used for EIS measurements, and the scan rate was 50 $mV{\cdot}s^{-1}$. Time-resolved fluorescence decay spectra were obtained using a LaserStrobe spectrofluorometer (PTI, Photon Technology International, Inc., USA) equipped with a nitrogen pumped dye laser as its light source, and the excitation wavelength of 465 nm was adopted in the measurements.

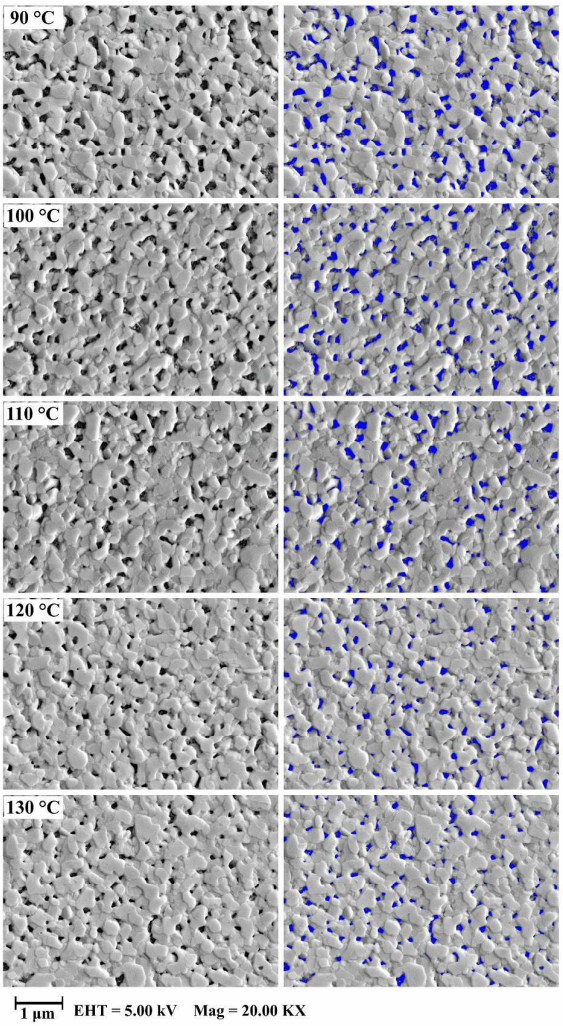

Fig. 1 The FE-SEM images of the PbI_2 films deposited on TiO_2 scaffold layer and heated at 90, 100, 110, 120 and 130 °C before and after filling the nanopores with blue colour.

Results and discussion

Morphology and coverage of PbI_2 thin film

In Fig. 1, the left five FE-SEM images display the surface morphologies of the PbI_2 thin films deposited on TiO_2 scaffold layers and heated at 90, 100, 110, 120 and 130 °C for 10 min, respectively. Fig. 1 shows that TiO_2 scaffold layers are covered with porous PbI_2 films, and the porous PbI_2 films are composed of PbI_2 nano-flakes connecting to each other. The dark regions in FE-SEM images could be identified as nanopores of PbI_2 films where the TiO_2 scaffold layer is uncovered. These five FE-SEM images also show that the size and density of nanopores of PbI_2 films both obviously decrease with the heating temperature increasing. After filling the nanopores with blue colour (the right five images of Fig. 1), the variation trend of the size and density of the nanopores with the heating temperature becomes more intuitive. It is obvious that reducing the nanopore size and density could increase the coverage of PbI_2 films. In order to further investigate the variation of nanopore size and density with the heating temperature of PbI_2 films, Image J2x software was used to analyze the FE-SEM images. For reducing the analytical error, three different magnification levels (5000×, 10000×, and 20000×) of FE-SEM images were used for analysis and the same threshold value was adopted in the binarization process. After binarization (the binarized images with different magnifications are shown in Fig. S1–S3), the average size and density of nanopores could be obtained using Image J2x software and the coverage of PbI_2 films could be estimated, the obtained data and corresponding curves are shown in Table 1 and Fig. 2, where the size of nanopores is represented by their average area. On the whole, the size and density of nanopores of PbI_2 films decrease obviously with the heating temperature increasing, and as a result, the coverage of PbI_2 films increases inevitably. Fig. 2B and Table 1 show that the coverage of PbI_2 films continuously increases with the heating temperature increasing. When the heating temperature increases to 130 °C, the coverage of PbI_2 films increases from

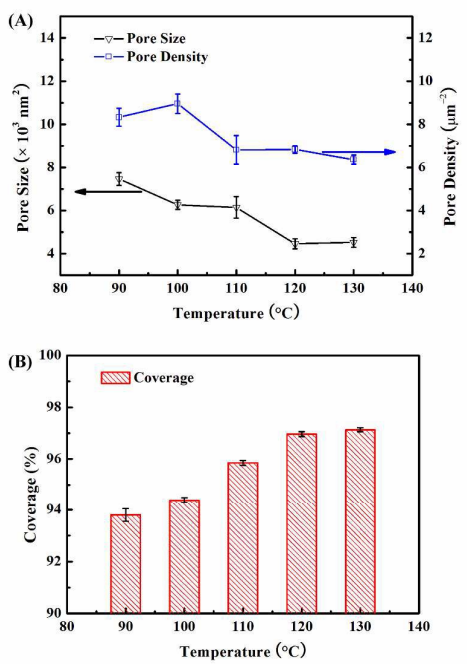

Fig. 2 The variation of (A) nanopore size and nanopore density and (B) coverage of PbI_2 films with the heating temperature.

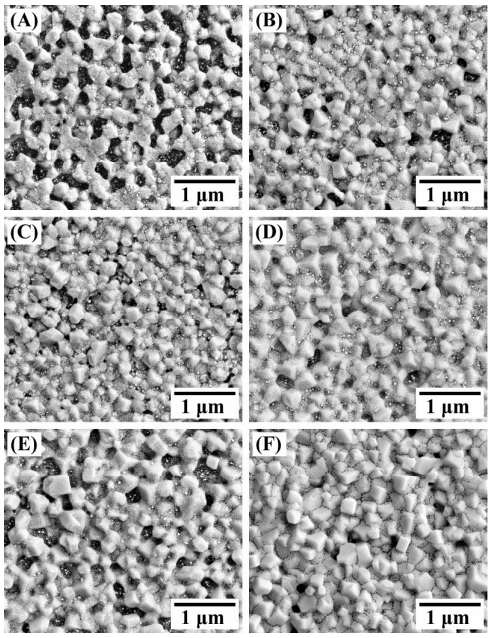

Fig. 3 The FE-SEM images of the $CH_3NH_3PbI_3$ films prepared at (A) 90/90 °C, (B) 100/100 °C, (C) 110/110 °C, (D) 120/120 °C, (E) 130/130 °C and (F) 130/120 °C.

Table 1 The nanopore size, nanopore density, and coverage of PbI_2 films prepared at different temperature.

Temperature (°C)	Nanopore Size ($\times 10^3$ nm^2)	Nanopore Density (μm^{-2})	Coverage (%)
90	7.47±0.30	8.33±0.41	93.80±0.25
100	6.26±0.21	8.96±0.45	94.40±0.10
110	6.14±0.50	6.82±0.66	95.85±0.09
120	4.46±0.23	6.84±0.17	96.96±0.09
130	4.52±0.23	6.37±0.21	97.13±0.08

93.80±0.25% (at 90 °C) to 97.13±0.08%. Furthermore, it is expectable that higher coverage PbI_2 films would lead to higher coverage $CH_3NH_3PbI_3$ films and more unreacted PbI_2 residue after reacting with CH_3NH_3I. And then, the charge recombination would be reduced and therefore the device performance would be improved.

Morphology and light absorption of $CH_3NH_3PbI_3$ films

Fig. 3 displays the FE-SEM images of $CH_3NH_3PbI_3$ films prepared at different temperature, where the preparation temperature has been written as *m*/*n* °C, *m* and *n* are the heating temperatures of PbI_2 and $CH_3NH_3PbI_3$ films, respectively. When the heating temperatures of PbI_2 and $CH_3NH_3PbI_3$ films are equal and the temperature ranges from 90/90 to 110/110 °C (Fig. 3A–C), it could be easily found that the size of $CH_3NH_3PbI_3$ nanoparticles is non-uniform and the average nanoparticle size slightly increases with the temperature increasing. Meanwhile, it is also obvious that the amount of nanopores decreases and the coverage of $CH_3NH_3PbI_3$ films increases with the temperature increasing. When the temperature reaches to 120/120 °C (Fig. 3D), the uniformity of $CH_3NH_3PbI_3$ nanoparticles has been improved obviously, the average size of $CH_3NH_3PbI_3$ nanoparticles and the coverage of $CH_3NH_3PbI_3$ films both further increase. When the temperature further reaches to 130/130 °C (Fig. 3E), the most notable feature is the obvious increase of the size and amount of the nanopores accompanied with the $CH_3NH_3PbI_3$ nanoparticle size continuously increasing, which leads to the obvious decrease of the coverage of $CH_3NH_3PbI_3$ films. This phenomenon indicates that higher temperature leads to larger $CH_3NH_3PbI_3$ nanoparticles and higher coverage $CH_3NH_3PbI_3$ films, and the coverage reaches the maximum value at 120/120 °C. The decrease of the coverage at 130/130 °C could be attributed to the partial decomposition of $CH_3NH_3PbI_3$ according to the previous investigations [39,40], and which has been proved by the XRD measurement. In order to further improve the morphology of $CH_3NH_3PbI_3$ films, some $CH_3NH_3PbI_3$ films were prepared at 130/120 °C (Fig. 3F), their compactness has been further improved compared with the $CH_3NH_3PbI_3$ films prepared at 120/120 °C.

XRD Patterns of a FTO substrate, a TiO_2 scaffold layer, a representative PbI_2 film heated at 100 °C, and the $CH_3NH_3PbI_3$ films prepared at different temperatures are shown in Fig. 4A. The XRD pattern of PbI_2 film indicates that the PbI_2 film is a pure PbI_2 film with hexagonal structure (JCPDS No. 73-1752) and good crystallinity. After reacting with CH_3NH_3I, the diffraction peaks of the obtained films agree well with the literature data on the tetragonal phase of $CH_3NH_3PbI_3$ [2]. However, the obtained films are not pure $CH_3NH_3PbI_3$ films, the (003) peak of hexagonal PbI_2 could be observed in the XRD pattern of each $CH_3NH_3PbI_3$ film. The relative intensity of (003) peak of PbI_2, defined as the intensity ratio of (003) peak of PbI_2

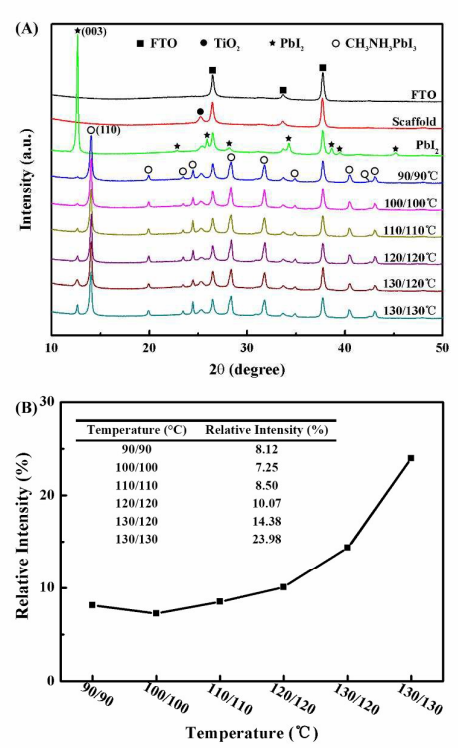

Fig. 4 (A) XRD Patterns of a FTO substrate, a TiO_2 scaffold layer, a representative PbI_2 film deposited on TiO_2 scaffold layer at 100 °C, and the $CH_3NH_3PbI_3$ films prepared at different temperatures. (B) The variation of relative intensity of (003) peak of PbI_2 with the preparation temperature. The relative intensity has been defined as the intensity ratio of (003) peak of PbI_2 to (110) peak of $CH_3NH_3PbI_3$.

to (110) peak of $CH_3NH_3PbI_3$ (at 14.0°, the strongest peak of $CH_3NH_3PbI_3$), has been used to analyze the mechanism of the presence of PbI_2 in $CH_3NH_3PbI_3$ films. Fig. 4B shows the variation of relative intensity of (003) peak of PbI_2 with the preparation temperature. The relative intensity of (003) peak of PbI_2 slightly increases from 7.25% to 10.07% with the temperature increasing from 100/100 to 120/120 °C, which could be attributed to the un-sufficient reaction of PbI_2 with CH_3NH_3I. The reaction of PbI_2 with CH_3NH_3I has occurred at room temperature, and the dense $CH_3NH_3PbI_3$ film on the surface of the PbI_2 film formed in the initial stage of the reaction may prevent the contact of PbI_2 with CH_3NH_3I and then affect sufficiency of the reaction [41]. When the temperature increases to 130/120 °C the relative intensity of (003) peak of PbI_2 further increases to 14.38%. When the temperature further increases to 130/130 °C, the relative intensity of (003) peak of PbI_2 sharply increases to 23.98%. The gradually increased relative intensity of (003) peak of PbI_2 indicates the content of PbI_2 in $CH_3NH_3PbI_3$ films increases with the temperature increasing, and the high relative intensity of 23.98% demonstrates that partial decomposition

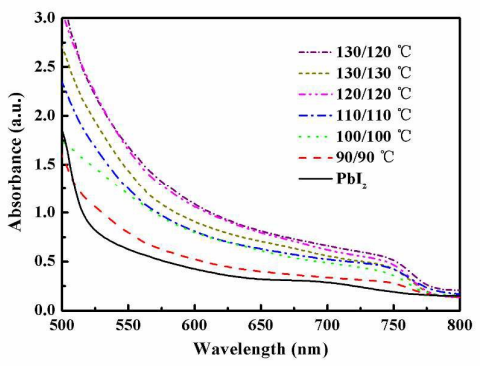

Fig. 5 UV–Vis–NIR absorbance spectra of the PbI_2 films prepared at 100 °C and the $CH_3NH_3PbI_3$ films prepared at different temperatures.

of $CH_3NH_3PbI_3$ has occurred at 130/130 °C according to the expression (1) [40].

$$CH_3NH_3PbI_3 \rightarrow PbI_2 + CH_3NH_2 + HI \quad (1)$$

As a result of the partial decomposition, the coverage of $CH_3NH_3PbI_3$ film decreases (Fig. 3E), and furthermore a decrease of light absorption would be inevitable. Additionally, the decomposited PbI_2 formed in the partial decomposition process of $CH_3NH_3PbI_3$ at 130/130 °C would fill the grain boundaries of $CH_3NH_3PbI_3$ and then retard the charge recombination.

Fig. 5 displays the UV–Vis–NIR absorbance spectra of the samples. The absorbance values of $CH_3NH_3PbI_3$ films increase over the whole spectral range with the temperature increasing from 90/90 to 120/120 °C, and the $CH_3NH_3PbI_3$ films prepared at 130/120 °C exhibits the strongest light absorption. When the temperature further increases to 130/130 °C the light absorption of $CH_3NH_3PbI_3$ films decreases obviously, which could be ascribed to the partial decomposition of $CH_3NH_3PbI_3$. Light-harvesting efficiency (LHE) has a positive correlation with the light absorption of the films, and therefore, stronger light absorption would lead to higher LHE, and higher LHE would lead to higher short-circuit current density (J_{sc}). Therefore, the maximum of J_{sc} would be obtained by the PSCs prepared at 130/120 °C.

Cell performance

The *J–V* curves and photovoltaic parameters of PSCs based on $CH_3NH_3PbI_3$ films prepared at different temperatures are shown in Fig. 6 and Table 2, respectively. Consistent with the expectation obtained from UV–Vis–NIR absorbance spectra, the J_{sc} increases with the temperature increasing from 90/90 to 130/120 °C, and further increasing the temperature to 130/130 °C decreases the J_{sc} of PSCs. The maximum J_{sc} of 20.66±0.43 mA·cm^{-2} is obtained by the PSCs prepared at 130/120 °C, and the corresponding open-circuit photovoltage (V_{oc}), fill factor (*FF*) and *PCE* are 960±7 mV, 70.4±0.5%, and 14.32±0.28%, respectively, which is the best performance of PSCs. The IPCE spectra of three representative PSCs prepared at 90/90, 120/120 and 130/120 °C, respectively, are shown in Fig. 7. The IPCE values of the PSCs

Table 2 The photovoltaic parameters of PSCs based on the $CH_3NH_3PbI_3$ films prepared at different temperatures. Each data is an average of ten samples.

Temperature (°C)	V_{oc} (mV)	J_{sc} (mA·cm^{-2})	*FF* (%)	*PCE* (%)
90/90	859 ± 10	11.66 ± 0.25	64.6 ± 0.2	6.48 ± 0.35
100/100	893 ± 4	12.23 ± 0.09	66.2 ± 0.4	7.23 ± 0.10
110/110	930 ± 5	15.79 ± 0.21	67.3 ± 0.3	9.89 ± 0.22
120/120	954 ± 8	18.83 ± 0.18	67.6 ± 0.1	12.15 ± 0.09
130/120	960 ± 7	20.66 ± 0.43	70.4 ± 0.5	14.32 ± 0.28
130/130	942 ± 4	18.00 ± 0.29	68.8 ± 0.4	11.67 ± 0.32

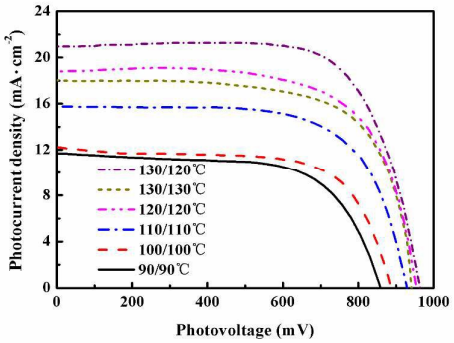

Fig. 6 *J–V* curves of PSCs based on the $CH_3NH_3PbI_3$ films prepared at different temperatures.

prepared at 120/120 °C are much higher than those of the PSCs prepared at 90/90 °C over the whole spectral range (300 – 800 nm), and the IPCE curve of the PSCs prepared at 130/120 °C is the highest one in the three PSCs, which means that the LHE of the $CH_3NH_3PbI_3$ films has been improved through increasing the preparation temperature from 90/90 to 120/120 °C, and the $CH_3NH_3PbI_3$ films prepared at 130/120 °C exhibit the highest LHE in the $CH_3NH_3PbI_3$ films prepared at different temperatures. Additionally, the integrated photocurrent density of the PSCs prepared at 90/90, 120/120 and 130/120 °C are 12.19, 18.52 and 20.02 mA·cm^{-2}, respectively, and they are consistent with the *J–V* results.

For PSCs prepared at 90/90, 100/100, 110/110, 120/120 and 130/130 °C, the variation of V_{oc} with the temperature is approximately consistent with that of J_{sc}, the V_{oc} increases with the temperature increasing and it reaches the maximum value of 954±8 mV at 120/120 °C. The variation of *FF* with the preparation temperature is different from that of J_{sc}, the *FF* increases with the temperature increasing from 90/90 to 130/130 °C, which means that the *FF* doesn't decrease with the partial decomposition of $CH_3NH_3PbI_3$ which is different from J_{sc}. The increase of *FF* is a positive factor for the cell performance, and the decrease of *PCE* at 130/130 °C is mainly attributed to the decrease of J_{sc} caused by the partial decomposition of $CH_3NH_3PbI_3$.

Passivation effect of the remnant PbI_2 in $CH_3NH_3PbI_3$ films

The dark current curves obtained through LSV measurement in the dark are displayed in Fig. 8, which shows that the onset of the dark current gradually increases with the temperature increasing from 90/90 to 130/130 °C. This phenomenon demonstrates that increasing preparation temperature could suppress the charge recombination in PSCs effectively and the suppression effect becomes more and more significant with the temperature increasing. As a result, the *FF* of PSCs has been gradually increased with the temperature increasing and subsequently the *PCE* has been also improved except the PSCs prepared at 130/130 °C.

EIS measurements exhibit the same results with LSV measurements. The representative Nyquist plots of PSCs prepared at 90/90, 100/100, 110/110, 120/120 and 130/130 °C obtained under the bias voltage of 0.8 V are shown in Fig. 9A. The obtained measurement data were fitted using Z-View software and a simplified equivalent circuit (the inset of Fig. 9A). Generally, a Nyquist plot consists of two semi arcs in the range of 10^6 – 1 Hz, the higher frequency arc is related to the diffusion resistance of holes through HTL, R_{HTL}, in parallel with HTL capacitance, CPE_{HTL}, and the lower frequency arc is related to the charge recombination at the ETL/perovskite interface and perovsktie/HTL interface, R_{rec}, in parallel with a chemical capacitance CPE_{rec} [42,43]. However, only the semi arc related to the charge recombination in every Nyquist plot could be observed in our measurements, and it is a recurring phenomenon according to the previous literatures [44,45].

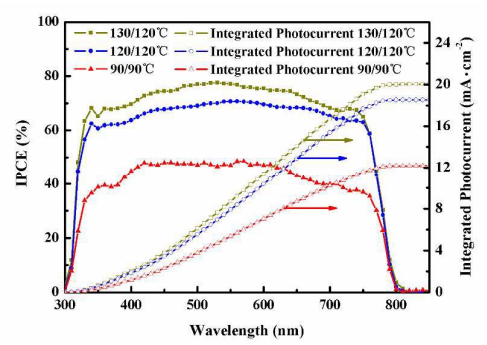

Fig. 7 (A) The IPCE spectra of three representative PSCs prepared at 90/90, 120/120 and 130/120 °C, respectively.

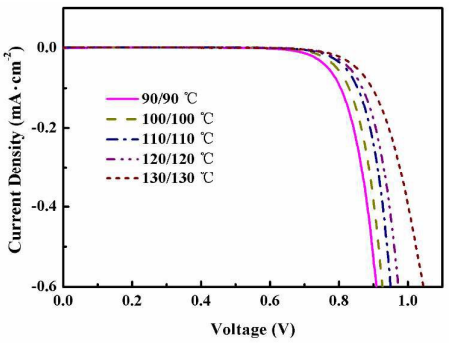

Fig. 8 Dark current–voltage curves of PSCs based on the $CH_3NH_3PbI_3$ films prepared at different temperatures.

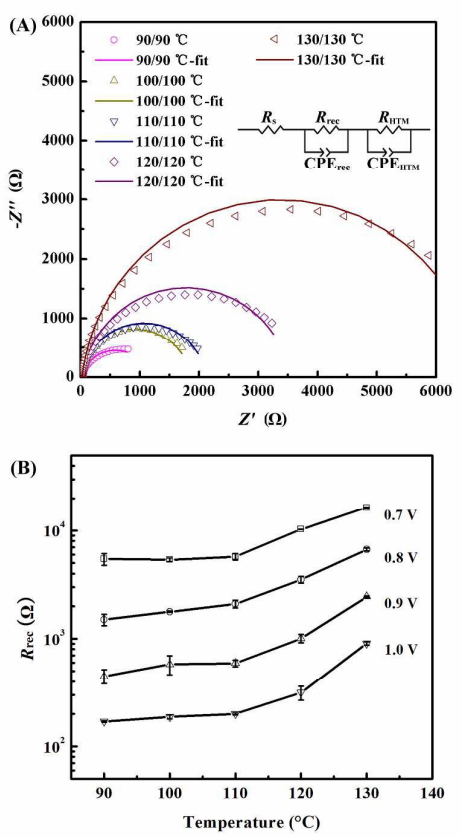

Fig. 9 (A) The representative Nyquist plots of PSCs prepared at different temperatures obtained under the bias voltage of 0.8V. (B) The variations of R_{rec} with the preparation temperature obtained under the bias voltages of 0.7, 0.8, 0.9 and 1.0 V.

Fig. 9A shows that the diameter of the semi arc increases with the preparation temperature increasing from 90/90 to 130/130 °C, and it significantly increases with the preparation temperature increasing from 120/120 to 130/130 °C, which indicates that increasing preparation temperature could increase the R_{rec} of PSCs, especially when the temperature increases from 120/120 to 130/130 °C. Additionally, the variations of R_{rec} with the preparation temperature obtained under the bias voltages of 0.7, 0.9 and 1.0 V shown in Fig. 9B are consistent with that of R_{rec} measured under 0.8 V (Fig. 9A). The enhanced R_{rec} suggests that the charge recombination in PSCs has been successfully suppressed through increasing the preparation temperature of PbI_2 and $CH_3NH_3PbI_3$ films.

What leads to the growing suppression of charge recombination with the preparation temperature increasing? Higher preparation temperature results in higher coverage PbI_2 films (Fig. 1) and higher coverage $CH_3NH_3PbI_3$ films (except the $CH_3NH_3PbI_3$ films prepared at 130/130 °C, Fig. 3). High coverage $CH_3NH_3PbI_3$ films could suppress charge recombination through reducing the detrimental direct contact between ETL and HTL. Meanwhile, higher coverage PbI_2 films would lead to more unreacted PbI_2 left (Fig. 4) and

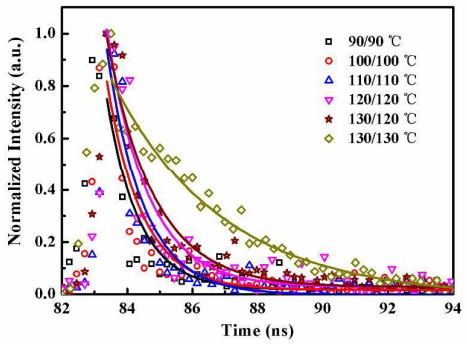

Fig. 10 Time-resolved fluorescence emission decay spectra and their fits (lines) of the $CH_3NH_3PbI_3$ films prepared at 90/90, 100/100, 110/110, 120/120, 130/120 and 130/130 °C.

Table 3 The emission lifetimes of the $CH_3NH_3PbI_3$ films prepared at 90/90, 100/100, 110/110, 120/120, 130/120 and 130/130 °C.

Temperature (°C)	τ (ns)	SE
90/90	0.98	0.13
100/100	1.08	0.13
110/110	1.12	0.11
120/120	1.25	0.13
130/130	3.39	0.29
130/120	1.44	0.12

located in the interface of ETL and $CH_3NH_3PbI_3$ layer, the contribution of the passivation effect of unreacted PbI_2 on suppressing charge recombination couldn't be excluded. When the temperature increases to 130/130 °C, the coverage of $CH_3NH_3PbI_3$ layer decreases obviously (Fig. 3E), but the suppression of charge recombination of PSCs are further enhanced (Fig. 8 and Fig. 9). What promotes the further suppression of charge recombination with the coverage of $CH_3NH_3PbI_3$ layer decreasing? It must definitely be the passivation effect of remnant PbI_2, particularly the decomposited PbI_2 formed in the partial decomposition process of $CH_3NH_3PbI_3$ sintered at 130 °C which could fill the grain boundaries of $CH_3NH_3PbI_3$ and then suppress the charge recombination at the perovsktie/HTL interface.

To further investigate the charge recombination behaviour and passivation effect of remnant PbI_2 in the PSCs, time-resolved fluorescence emission decay measurements were performed on the samples of FTO/ETL/$CH_3NH_3PbI_3$ films prepared at different temperatures, and the emission lifetime could be obtained through fitting the fluorescence emission decay spectra using exponential function. The FTO/ETL/$CH_3NH_3PbI_3$ films without HTL Layers could avoid the charge recombination at $CH_3NH_3PbI_3$/HTL interface, and the corresponding fluorescence emission lifetime would reflects the charge recombination behaviour at ETL/$CH_3NH_3PbI_3$ interface and the $CH_3NH_3PbI_3$ grain boundaries, longer emission lifetime would indicate the enhanced suppression of the charge recombination. Fig. 10 shows the time-resolved fluorescence emission decay spectra and Table 3 displays the corresponding lifetime of the samples. The lifetime gradually

increases from 0.98 ns at 90/90 °C to 1.25 ns at 120/120 °C, and further to 1.44 ns at 130/120 °C. Considering that the content of unreacted PbI_2 in the $CH_3NH_3PbI_3$ films gradually increases with the temperature increasing from 90/90 °C to 120/120 °C and further to 130/120 °C (XRD results, Fig. 4), the increase of the emission lifetime could be ascribed to the increasing passivation effect of the unreacted PbI_2 located between the ETL and $CH_3NH_3PbI_3$ layers which suppresses the charge recombination at the ETL/perovskite interface. This result is an evidence for the passivation effect of the unreacted PbI_2 located between the ETL and $CH_3NH_3PbI_3$ layers, and which improves the cell performance of PSCs obviously (Table 2 and Fig. 6). Furthermore, when temperature increases to 130/130 °C, partial decomposition of $CH_3NH_3PbI_3$ has occurred, the emission lifetime sharply increases to 3.39 ns, which could be attributed to the decomposited PbI_2 filling the $CH_3NH_3PbI_3$ grain boundaries and further suppressing the charge recombination. This is a powerful evidence for the passivation effect of the docomposited PbI_2 in the $CH_3NH_3PbI_3$ films. Although the *PCE* of PSCs prepared at 130/130 °C is lower than that of PSCs prepared at 120/120 °C and 130/120 °C caused by the partial decomposition of $CH_3NH_3PbI_3$, the charge recombination has been suppressed effectively, and optimizing the amount and location of the docomposited PbI_2 would inevitably improve the device performance of PSCs.

So far, the passivation effects of the unreacted and decomposited PbI_2 have been confirmed unquestionably, and the passivation effect of the unreacted PbI_2 has been proven to improve the cell performance of the PSCs. In the future, more efforts should be devoted to optimize the amount, location and form of the remnant PbI_2 in $CH_3NH_3PbI_3$ films for further improving the device performance of PSCs.

Conclusions

In summary, the $CH_3NH_3PbI_3$ films were obtained by two-step spin-coating method and the content of the remnant PbI_2 in $CH_3NH_3PbI_3$ films was tuned through varying the preparation temperature. Increasing the heating temperature could increase the coverage of spin-coated PbI_2 films, which resulted in high coverage $CH_3NH_3PbI_3$ films and more remnant PbI_2 in $CH_3NH_3PbI_3$ films. As a result, the cell performance of PSCs was enhanced obviously, and a relatively high *PCE* of 14.32±0.28% was achieved by the PSCs prepared at 130/120 °C. Furthermore, the charge recombination in PSCs was effectively suppressed with the content of remnant PbI_2 increasing, and the passivation effects of the unreacted and decomposited PbI_2 for improving the performance of PSCs have been confirmed unquestionably. In the future, further optimizing the content, location and form of the remnant PbI_2 in $CH_3NH_3PbI_3$ films is a feasible approach for the improvement of the device performance of PSCs.

Acknowledgements

This work was supported by the National Natural Science Foundation of China (51172237, 61306082, 61306083), the China Postdoctoral Science Foundation (2014M561845), Anhui Provincial International Science and Technology Cooperation Program (10080703021), and Anhui Provincial Key Lab of Photonics Devices and Materials.

Notes and references

1 J.-H. Im, C.-R. Lee, J.-W. Lee, S.-W. Park, N.-G. Park, *Nanoscale*, 2011, **3**, 4088.
2 T. Baikie, Y. Fang, J. M. Kadro, M. Schreyer, F. Wei, S. G. Mhaisalkar, M. Grätzel, T. J. White, *J. Mater. Chem. A*, 2013, **1**, 5628.
3 C. S. Ponseca Jr., T. J. Savenije, M. Abdellah, K. Zheng, A. Yartsev, T. Pascher, T. Harlang, P. Chabera, T. Pullerits, A. Stepanov, J.-P. Wolf, V. Sundström, *J. Am. Chem. Soc.*, 2014, **136**, 5189.
4 D. B. Mitzi, *J. Chem. Soc., Dalton Trans.*, 2001, **1**, 1.
5 C. C. Stoumpos, C. D. Malliakas, M. G. Kanatzidis, *Inorg. Chem.*, 2013, **52**, 9019.
6 G. Xing, N. Mathews, S. Sun, S. S. Lim, Y. M. Lam, M. Grätzel, S. Mhaisalkar, T. C. Sum, *Science*, 2013, **342**, 344.
7 S. D. Stranks, G. E. Eperon, G. Grancini, C. Menelaou, M. J. P. Alcocer, T. Leijtens, L. M. Herz, A. Petrozza, H. J. Snaith, *Science*, 2013, **342**, 341.
8 E. J. W. Crossland, N. Noel, V. Sivaram, J. A. Alexander-Webber, H. J. Snaith, *Nature*, 2013, **495**, 215.
9 M. Grätzel, *Nat. Mater.*, 2014, **13**, 838.
10 S. Pang, H. Hu, J. Zhang, S. Lv, Y. Yu, F. Wei, T. Qin, H. Xu, Z. Liu, G. Gui, *Chem. Mater.*, 2014, **26**, 1485.
11 W. S. Yang, J. H. Noh, N. J. Jeon, Y. C. Kim, S. Ryu, J. Seo, S. I. Seok, *Science*, 2015, **348**, 1234.
12 C. Li, F. Wang, J. Xu, J. Yao, B. Zhang, C. Zhang, M. Xiao, S. Dai, Y. Li, Z. Tan, *Nanoscale*, 2015, **7**, 9771.
13 A. Kojima, K. Teshima, Y. Shirai, T. Miyasaka, *J. Am. Chem. Soc.*, 2009, **131**, 6050.
14 NREL, Research Cell Efficiency Records, http://www.nrel.gov/ncpv/images/efficiency_chart.jpg, accessed 16 Jan. 2016.
15 J. Shi, X. Xu, D. Li, Q. Meng, *Small*, 2015, **11**, 2472.
16 L. Zheng, D. Zhang, Y. Ma, Z. Lu, Z. Chen, S. Wang, L. Xiao, Q. Gong, *Dalton Trans.*, 2015, **44**, 10582.
17 T. Salim, S. Sun, Y. Abe, A. Krishna, A. C. Grimsdale, Y. M. Lam. *J. Mater. Chem. A*, 2015, **3**, 8943.
18 Y. Zhou, A. L. Vasiliev, W. Wu, M. Yang, S. Pang, K. Zhu, N. P. Padture, *J. Phys. Chem. Lett.*, 2015, **6**, 2292.
19 H.-L. Hsu, C.-P. Chen, J.-Y. Chang, Y.-Y.Yu, Y.-K. Shen, *Nanoscale*, 2014, **6**, 10281.
20 G. E. Eperon, V. M. Burlakov, P. Docampo, A. Goriely, H. J. Snaith, *Adv. Funct. Mater.*, 2014, **14**, 151.
21 Y. Zhou, M. Yang, A. L. Vasiliev, H. F. Garces, Y. Zhao, D. Wang, S. Pang, K. Zhu, N. P. Padture, *J. Mater. Chem. A*, 2015, **3**, 9249.
22 D. Wang, Z. Liu, Z. Zhou, H. Zhu, Y. Zhou, C. Huang, Z. Wang, H. Xu, Y. Jin, B. Fan, S. Pang, G. Cui, *Chem. Mater.*, 2014, **26**, 7145.
23 J. Burschka, N. Pellet, S.-J. Moon, R. Humphry-Baker, P. Gao, M. K. Nazeeruddin, M. Grätzel, *Nature,* 2013, **499**, 316.
24 C. Ying, C. Shi, N. Wu, J. Zhang, M. Wang, *Nanoscale*, 2015, **7**, 12092.
25 L. Yang, J. Wang, W. W.-F. Leung, *ACS Appl. Mater. Interfaces*, 2015, **7**, 14614.
26 J. Song, E. Zheng, J. Bian, X.-F. Wang, W. Tian, Y. Sanehira, T. Miyasaka, *J. Mater. Chem. A*, 2015, **3**, 10837

27 V. Somsongkul, F. Lang, A. R. Jeong, M. Rusu, M. Arunchaiya, T. Dittrich, *Phys. Status Solidi PRL*, 2014, **8**, 763.
28 D. H. Cao, C. C. Stoumpos, C. D. Malliakas, M. J. Katz, O. K. Farha, J. T. Hupp, M. G. Kanaatzidis, *APL Mater.*, 2014, **2**, 091101.
29 T. Supasai, N. Rujisamphan, K. Ullrich, A. Chemseddine, T. Dittrich, *Appl. Phys. Lett.*, 2013, **103**, 183906.
30 Q. Chen, H. Zhou, T.-B. Song, S. Luo, Z. Hong, H.-S Duan, L. Dou, Y. Liu, Y. Yang, *Nano Lett.*, 2014, **14**, 4158.
31 L. Wang, C. McCleese, A. Kovalsky, Y. Zhao, C. Burda, *J. Am. Chem. Soc.*, 2014, **136**, 12205.
32 D. Bi, W. Tress, M. I. Dar, P. Gao, J. Luo, C. Renevier, K. Schenk, A. Abate, F. Giordano, J.-P. C. Baena, J.-D. Decoppet, S. M. Zakeeruddin, M. K. Nazeeruddin, M. Grätzel, A. Hagfeldt, *Sci. Adv.*, 2016, **2**, e1501170.
33 D. Bi, A. M. El-Zohry, A. Hagfeldt, G. Boschloo, *ACS Photonics*, 2015, **2**, 589.
34 H. Zhang, J. Mao, H. He, D. Zhang, H. L. Zhu, F. Xie, K. S. Wong, M. Grätzel, W. C. H. Choy, *Adv. Energy Mater.*, 2015, **5**, 1501354.
35 Y. Xie, F. Shao, Y. Wang, T. Xu, D. Wang, F. Huang, *ACS Appl. Mater. Interfaces*, 2015, **7**, 12937.
36 F. Liu, Q. Dong, M. K. Wong, A. B. Djurišić, A. Ng, Z. Ren, Q. Shen, C. Surya, W. K. Chan, J. Wang, A. M. C. Ng, C. Liao, H. Li, K. Shih, C. Wei, H. Su, J. Dai, *Adv. Energy Mater.,* 2016, DOI: 10.1002/aenm.201502206.
37 J.-H. Im, I-H. Jang, N. Pellet, M. Grätzel, N.-G. Park, *Nat. Nanotechnol.*, 2014, **9**, 927.
38 A. Abrusci, S. D. Stranks, P. Docampo, H.-L. Yip, A. K.-Y. Jen, H. J. Snaith, *Nano Lett.*, 2013, **13**, 3124.
39 B. Tripathi, P. Bhatt, P. C. Kanth, P. Yadav, B. Desai, M. K. Pandey, M. Kumar, *Sol. Energy Mat. Sol. Cells*, 2015**, 132**, 615.
40 A. Dualeh, N. Tétreault, T. Moehl, P. Gao, M. K. Nazeeruddin, M. Grätzel, *Adv. Funct. Mater.*, 2014, **24**, 3250.
41 G. Murugadoss, G. Mizuta, S. Tanaka, H. Nishino, T. Umeyama, H. Imahori, S. Ito, *APL Mater.*, 2014, **2**, 081511.
42 J. A. Christinans, R. C. M. Fung, *J. Am. Chem. Soc.*, 2014, **136**, 758.
43 A. Dualeh, T. Moehl, N. Tétreault, J. Teuscher, P. Gao, M. K. Nazeeruddin, M. Grätzel, *ACS Nano*, 2014, **8**, 362.
44 L. Zhu, J. Shi, S. Lv, Y. Yang, X. Xu, Y. Xu, J. Xiao, H. Wu, Y. Luo, D. Li, Q. Meng, *Nano Energy*, 2015, **15**, 540.
45 Y. Li, J. Zhu, Y. Huang, J. Wei, F. Liu, Z. Shao, L. Hu, S. Chen, S. Yang, J. Tang, J. Yao, S. Dai, *Nanoscale*, 2015, **7**, 9902.